Front. Energy 2020, 14(1): 18–26
https://doi.org/10.1007/s11708-020-0663-6

RESEARCH ARTICLE

Wang LIU, Jiaqi ZHAI, Baiyang LIN, He LIN, Dong HAN

Soot size distribution in lightly sooting premixed flames of benzene and toluene

Abstract The evolution of particle size distribution function (PSDF) of soot in premixed flames of benzene and toluene was studied on a burner stabilized stagnation (BSS) flame platform. The cold gas velocities were changed to hold the maximum flame temperatures of different flames approximately constant. The PSDFs of all the test flames exhibited a bimodal distribution, i.e., a small-size nucleation mode and a large-size accumulation mode. It was observed that soot nucleation and particle growth in the benzene flame were stronger than those in the toluene flame at short residence times. At longer residence times, the PSDFs of the two flames were similar, and the toluene flame showed a larger particle size distribution range and a higher particle volume fraction than the benzene flame.

Keywords premixed flame, soot, particle size distribution function, benzene, toluene

1 Introduction

Haze pollution is regarded as a global environmental threat caused by human activities. Particulate matter (PM), a primary pollutant in haze pollution [1], mainly originates from fossil fuel combustion in various industrial processes [2–4]. For the past decades, many countries have been publishing increasingly stringent regulations for PM emissions control. For example, the limits of PM emissions for diesel passenger cars was reduced from 0.14 g/km (Euro I, 1992) to 0.05 g/km (Euro VI, 2014) in Europe [5,6]. Therefore, researches investigating the sooting processes in fuel combustion were widely concerned.

Received Aug. 10, 2019; accepted Oct. 22, 2019; online Jan. 26, 2020

Wang LIU, Jiaqi ZHAI, Baiyang LIN, He LIN, Dong HAN (✉)
Key Laboratory for Power Machinery and Engineering, Ministry of Education, Shanghai Jiao Tong University, Shanghai 200240, China
E-mail: dong_han@sjtu.edu.cn

Soot formation tendency in combustion processes was found to be strongly dependent on fuel compositions [7–9]. Particularly, it was generally believed that the aromatic components contributed to soot formation in engine combustion [10], as aromatics had a higher poly condensation tendency. Sobotowski et al. [11] found that large-molecule aromatics had strong influences on soot emissions from gasoline vehicles. DeWitt et al. [12] and Short et al. [13] also revealed that that increased aromatics fraction in fuels increased soot emissions from gasoline engines. Since aromatic hydrocarbons are important components in gasoline and diesel, extensive studies have been conducted, aiming to elucidate the correlation between fuel aromatics and soot formation tendency [14–17].

In the last several decades, researchers have tried to identify the soot formation processes in aromatics flames based on different experimental methods. Camacho [18] investigated the surface oxidation rate of nascent soot in the flames of benzene and several C_6 hydrocarbons in a novel aerosol flow reactor. The fastest onset of soot nucleation was observed in the benzene flames due to significant formation of PAHs in the pre-flame region. Simmons and Williams [19] studied the rate of soot formation for benzene, toluene, and toluene/n-heptane mixtures using a reflected shock tube. They found that the rates of soot formation and soot yields exhibited an Arrhenius dependence. Ergut et al. [20] investigated the equivalence ratio effects on the soot onset chemistry in premixed ethyl benzene flames. Gas chromatography coupled with mass spectrometry was used to analyze the concentrations of soot, polycyclic aromatic hydrocarbons, and oxygenated species in the samples. The results showed that the soot onset limit was expanded as equivalence ratio increased.

Recently, probe sampling technique coupled with particle size distribution function (PSDF) measurement enabled quantitative analysis of the nascent soot particle size distribution features in flames [21–26]. Nascent soot particles were sampled and immediately diluted by cold

nitrogen, minimizing the particle losses in the sampling processes. Maricq [22] compared the PSDFs in premixed benzene/ethylene mixtures and other hydrocarbon flames. He found that the soot particle size distributions were sensitive to the fuel molecular structure, the flame gas velocity, and the sampling dilution ratio. Tang et al. [23] investigated the PSDFs of n-heptane/toluene mixtures based on a BSS platform. They indicated that soot inception occurred at lower flame heights and the particle size distribution range was significantly reduced with the addition of toluene. Abid et al. [24] measured the PSDFs of ethylene/benzene mixtures to identify the effects of benzene concentration on the evolution of soot size distribution. They found that the addition of less than 2% of benzene to ethylene had little effects on the nascent soot when the C/O ratio was kept constant. However, Echavarria et al. [25] observed that a higher benzene proportion in the ethylene/benzene mixture caused a higher soot nucleation and accumulation rate, especially at high flame temperatures. Lin et al. [26] compared the evolution of PSDFs in premixed flames of practical gasoline (34% aromatics by volume) and a binary gasoline surrogate of 66% n-heptane and 34% toluene by volume, and observed that gasoline featured more persistent nucleation and much faster particle growth rate.

In this paper, the evolution of PSDFs in premixed benzene and toluene flames was studied on the BSS flame. Since benzene and toluene are regarded as the typical surrogates of aromatics, the study on their sooting tendencies could facilitate the understanding of the soot generation mechanism of aromatic fuels and lay the foundation for the soot formation study of aromatics with more complicated molecular structures.

2 Experimental method

The schematic of the experimental setup is shown in Fig. 1. An atmospheric premixed flame of fuel/oxygen/nitrogen was stabilized on a height-adjustable burner for particle formation and sampling. The burner consisted of a porous plug with a diameter of 5 cm and a concentric porous ring. A shielding nitrogen flow through the concentric ring was used to isolate the flames and the ambient environment. The fuel flow rate was adjusted by a syringe pump (Harvard PHD 2000 Series) and the liquid fuel was atomized through a nebulizer (Precision Glassblowing, Glass Concentric Nebs). A constant temperature of 150°C was maintained in the gas pipes and the burner to avoid fuel condensation, which was achieved by heating tapes.

An S-type thermocouple was used to measure the centerline temperature profiles in the flames. The thermocouple was coated with the YCl_3/BeO mixture to minimize radiation losses and prevent catalytic reaction in the flames. The coated wire and bead were 0.14 mm and 0.28 mm in diameter, respectively. The burner surface temperature was linearly extrapolated from the measured values close to the burner due to the difficulty in the surface temperature measurement by the thermocouple. Radiation correction was carried out based on the Shaddix procedure [27], with an upper/lower emissivity limit of 0.6/0.3, respectively [28]. The average value of the temperatures

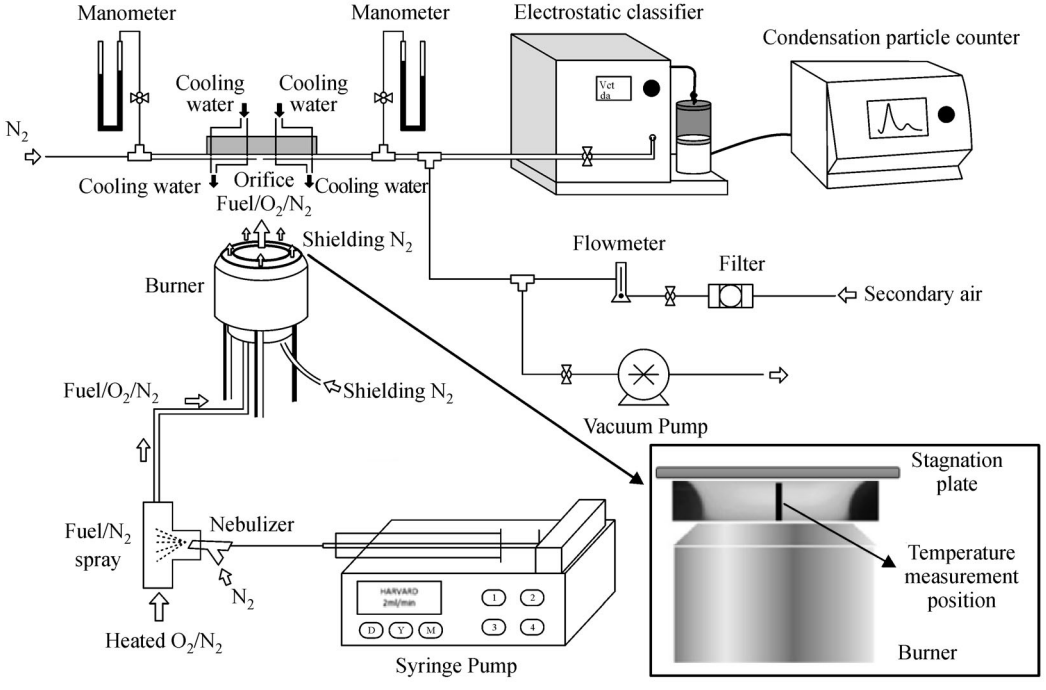

Fig. 1 Schematic of experimental setup.

corrected by the two emissivity limits was assumed to be the radiation-corrected temperature [26,27,29,30]. The centerline temperature distributions above the burner were also calculated based on the modified OPPDIF code [31–33]. The fuel mole fraction, the height, and the mass flow rate of gas mixtures were inputs in the OPPDIF code. GRAD and CURV were set as 0.1 and 0.2, respectively.

The stagnation surface temperature was measured by a K-type thermocouple. The sampling plate was composed of a water-cooled stagnation plate and a stainless-steel sampling tube embedded into the plate. The outer diameter of the sampling tube was 6.35 mm and the wall thickness was 0.127 mm. The sampling orifice of the tube was 0.13 mm in diameter, which was located at the same height as the stagnation surface. To avoid blockage, a stainless needle was used to clean the orifice after each sample. The sampled soot particles were then diluted by a cold nitrogen flow (30 L/min, at STP condition). The dilution ratio was calibrated by using the bubble flowmeter method [34,35]. For each test condition, a set of PSDFs were recorded at different dilution ratios. Then, an optimal range of dilution ratio was determined to ensure that the dilution-corrected PSDF was insensitive to the dilution ratio. The diluted sample was then analyzed by a TSI Scanning Mobility Particle Sizer (SMPS) including an Electrostatic Classifier (EC, model 3080) and an ultra-fine Condensation Particle Counter (CPC, model 3776). The EC consists of a nano Differential Mobility Analyzer (DMA, model 3085) and a Kr-85 Particle Neutralizer. With a scanning time of 30 s up and 10 s retrace, the distribution function for particle size from 2.5 to 66.1 nm was obtained. The premixed gases were composed of 60% molar-basis nitrogen as the carrier gas and certain proportions of fuel/oxygen to attain the target equivalence ratios under all test conditions. The largest separation distance from the burner to the stagnation surface was 1.6 cm. Table 1 lists the detailed test conditions in this study.

3 Results and discussion

The temperature distributions along the centerline for the two flames were measured at different heights to eliminate the effects of flame temperature on particle generation. Figure 2 demonstrates the comparisons between the computed and measured centerline temperature profiles for the two flames. For either flame, burner-to-stagnation surface separations (H_p) of 1.0 cm, 1.2 cm, 1.4 cm and 1.6 cm were selected. The symbols represent the radiation-corrected temperatures and the lines are the simulated centerline temperatures based on the modified OPPDIF code. The horizontal error bars indicate the uncertainties of the thermocouple position caused by the bead radius of the coated thermocouple. The vertical error bars represent the effects of emissivity uncertainty in the radiation correction. It is seen that the computed axial temperature profiles agree well with the radiation-corrected temperatures. The maximum temperatures at different H_ps were similar, suggesting that H_p had little effects on the maximum temperatures.

Particle residence time is defined as the time interval for the particle transporting from the position of the calculated maximum flame temperature to the stagnation plate. It is an important parameter in soot particle formation, whose equation is

$$t = \int_{x_{T_m}}^{H_p} \frac{\mathrm{d}x}{v_c(x) + v_T(x)}, \tag{1}$$

where x is the axial position above the burner, x_{T_m} is the location of the maximum flame temperature, $v_c(x)$ is the convective velocity determined by the OPPDIF non-slip boundary solution, and $v_T(x)$ is the thermophoretic velocity, defined as [36]

$$v_T = \frac{\lambda}{5(1 + \pi\varphi/8)Nk_B T}\frac{\mathrm{d}T}{\mathrm{d}x}, \tag{2}$$

where λ is the thermal conductivity calculated from the transport properties of the flame gas in the multi-component formulation, T is the flame temperature, N is the number density of the gas molecules, k_B is the Boltzmann constant, and φ is the momentum accommodation factor set to be 0.9 [37]. However, the sample taken represents an average of the gas volume immediately adjacent to the orifice due to the low-pressure nitrogen flow. Such a gas volume could be represented by shifting the spatial position of the probe about 1 mm toward the burner [26,27,30,31]. Therefore, the modified residence time is

$$t' = \int_{x_{T_m}}^{H_p - 0.1\,\mathrm{cm}} \frac{\mathrm{d}x}{v_c(x) + v_T(x)}. \tag{3}$$

It is known to all that soot particles evolve with residence time. Therefore, the PSDFs were compared at

Table 1 Test flame conditions

Flame	Mole fraction			Cold gas velocity $v_0/(\mathrm{cm\cdot s^{-1}})^a$	Maximum temperature T_m/K^b	Stagnation surface temperature T/K^b	ϕ	C/O ratio
	Fuel	O_2	N_2					
Benzene(B)	0.0757	0.3243	0.6000	4.4	1872±86	406	1.75	0.70
Toluene (T)	0.0651	0.3349	0.6000	3.6	1875±87	393	1.75	0.68

Notes: [a]—At STP condition (298 K and 1 atm); [b]—Measured for the largest burner-to-stagnation surface separation; $H_{p,\max}$ = 1.6 cm for the two flames.

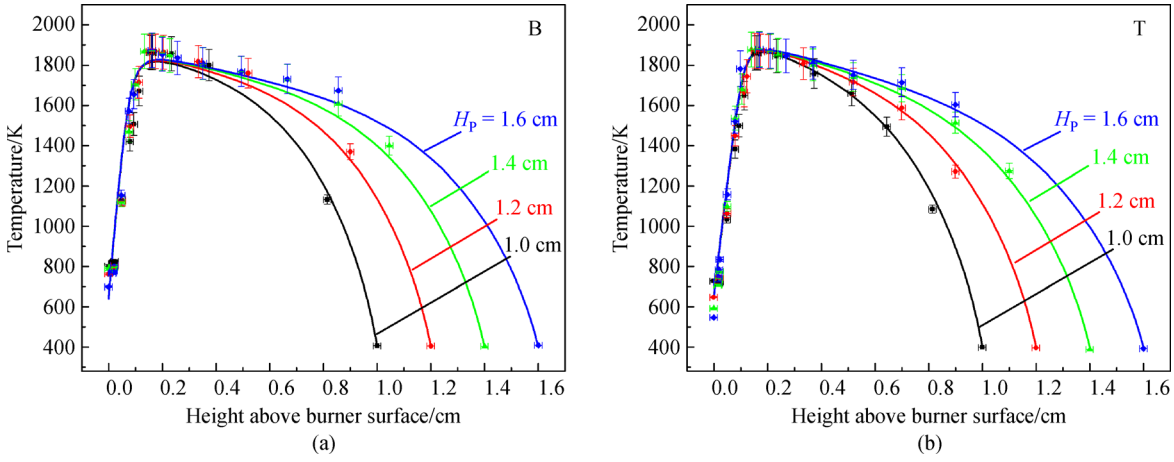

Fig. 2 Measured (symbols) and computed (lines) centerline temperature profiles for the two flames. (a) The benzene flame; (b) the toluence flame.

similar particle residence times for the two flames. For each flame, four sets of H_ps were selected for PSDF measurements. The corresponding modified residence times are fixed at around 45, 60, 75, and 90 ms, respectively, as displayed in Table 2.

Figure 3 exhibits the simulated temperature-time histories of the two flames at the selected particle residence times. It is observed that the temperature-time histories of both fuels are similar for each set of residence time. Since the flame temperature is an important factor affecting soot nucleation and particle growth, the consistency in temperature-time histories lays the foundation for the PSDF comparison of the two flames.

Table 2 Burner-to-stagnation separations and the corresponding particle residence times

Flame	Burner-to-stagnation separation H_p/cm	Modified residence time t' (ms, at $H_p-0.1$cm)
B	0.98	44.7
	1.18	59.6
	1.37	75.3
	1.56	90.5
T	0.92	45.4
	1.10	60.4
	1.27	75.7
	1.42	90.2

The measured PSDFs for the two flames are plotted in Fig. 4. The horizontal axis D_m represents the mobility diameter, which is the diameter of a spherical particle with the same electrical mobility as the sampled particle. The vertical axis $dN/d\log(D_m)$ represents the number density of soot particles for a certain D_m. All the PSDFs are observed to be bimodal distribution, with the small-size nucleation mode and the large-size accumulation mode. As is depicted by the lines in Fig. 4, all the particle size distributions can be fitted by a bi-lognormal distribution function [38] as

$$\frac{dN}{d\log D_m} = \Sigma_{i=1}^{2} \frac{N_i}{\sqrt{2\pi}\log\sigma_{g,i}} \exp\left\{-\frac{\log(D_m/\langle D_{m,i}\rangle)^2}{2(\log\sigma_{g,i})}\right\}, \quad (4)$$

where N is the number density, σ_g is the geometric standard deviation, and $\langle D_m \rangle$ is the median mobility diameter. In Eq. (4), the nucleation mode is defined as $i = 1$ and the accumulation mode is labeled as $i = 2$.

Figure 4 illustrates particle size distributions at different heights for benzene and toluene. At low heights, the nucleation mode is stronger and a large number of small particles are produced. With increased heights, the number densities of the nucleation modes decrease in both flames, because increased particle accumulation consumes a large number of small-size particles. For either flame, the trough is regarded as the coupling of the nucleation and accumulation modes and the location of the trough reflects their competition. The decreased number density of small particles and increased number density of large particles results in an obvious occurrence of the trough.

Figure 5 presents the PSDFs comparison of the two flames at the same residence time. At short residence times as 45 and 60 ms, the B flame exhibits a higher accumulation tendency and a wider distribution range than the T flame. As the residence time increases to over 75 ms, the accumulation tendency of the T flame is close to that of the B flame. It is also noticeable that the B flame has a larger mobility diameter at the PSDF trough than the T flame at the residence time of over 60 ms, indicating that the B flame has a larger nucleation strength in bimodal PSDFs. As a result, at a short residence time of about 45 ms, the PSDF of the B flame shows a bimodal distribution, while that of the T flame only exhibits a unimodal distribution. At the residence time of above 75 ms, the PSDFs of B and T flames are similar.

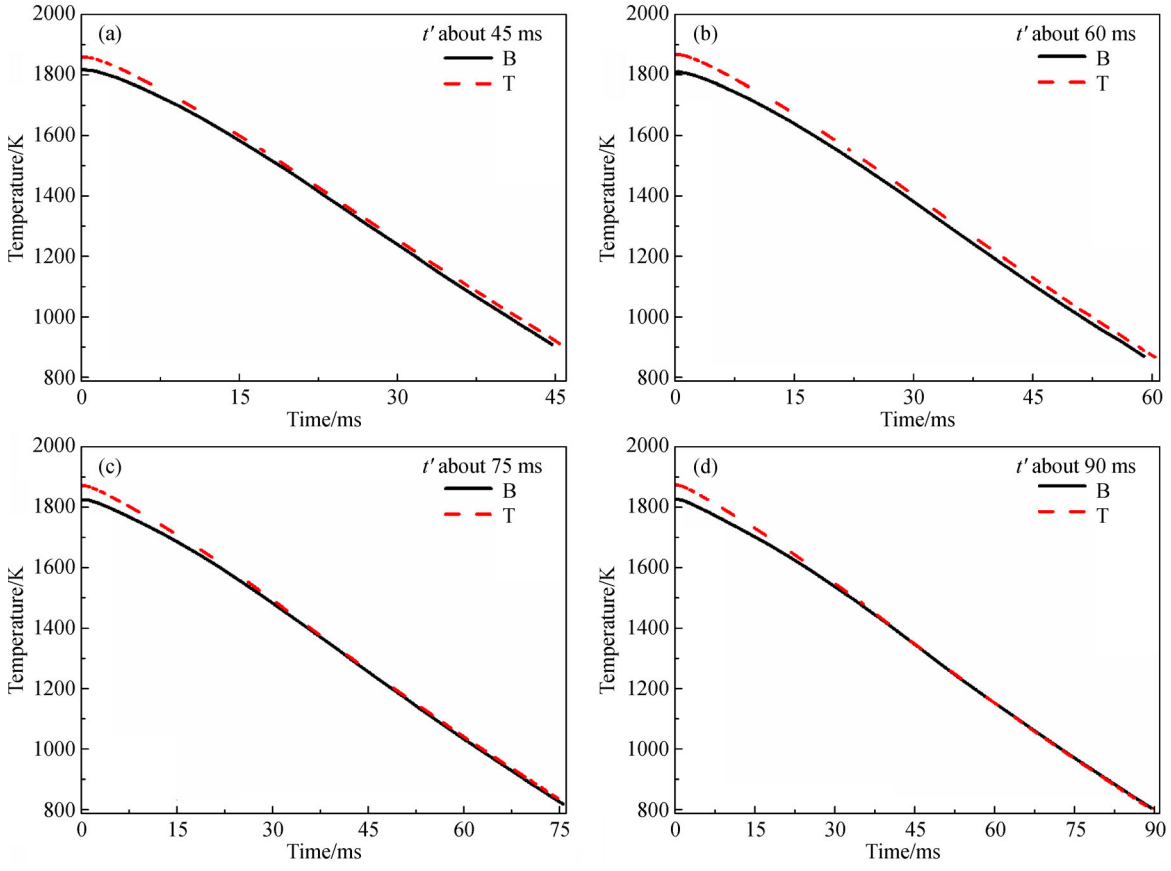

Fig. 3 Temperature-time histories calculated at two particle residence times.

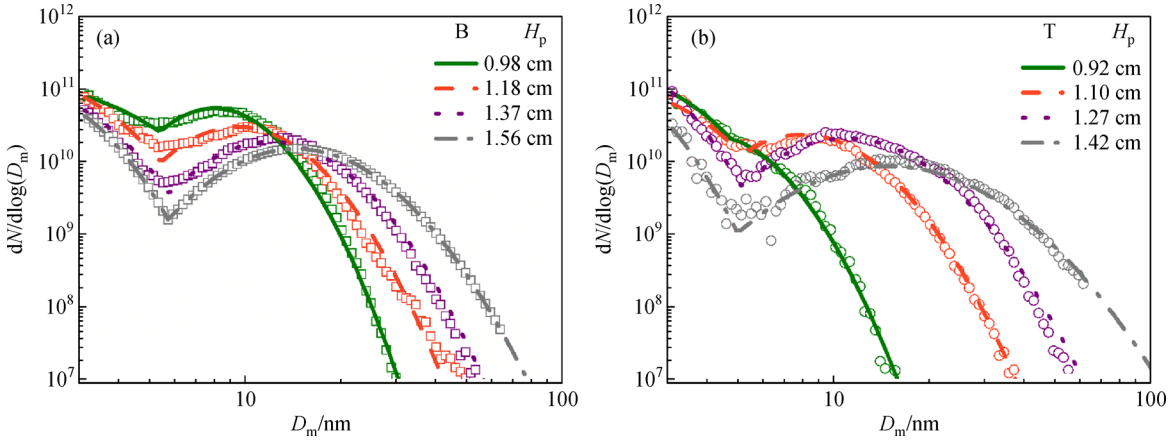

Fig. 4 Measured PSDFs for the two flames (a) The benzene flame; (b) the toluence flame. (Symbols: experimental data; lines: bi-lognormal fits to data).

Some critical parameters are derived from the PSDFs for further comparison. The total particle number densities of each flame at different particle residence times are presented in Fig. 6. The value of total number density N is calculated based on the following integration:

$$N = \int_{D_{m,min}}^{D_m} \frac{dN}{d\log D_m} d\log D_m, \quad (5)$$

where only particles whose mobility diameters are higher than 2.5 nm and the $dN/d\log(D_m)$ are higher than 10^6 are taken into consideration. The contribution of these particles to number density is estimated by the bi-lognormal distribution function fits. At short particle residence times, the total number density of the T flame increases as the particle residence time increases. The consumption of small-size particles by particle accumula-

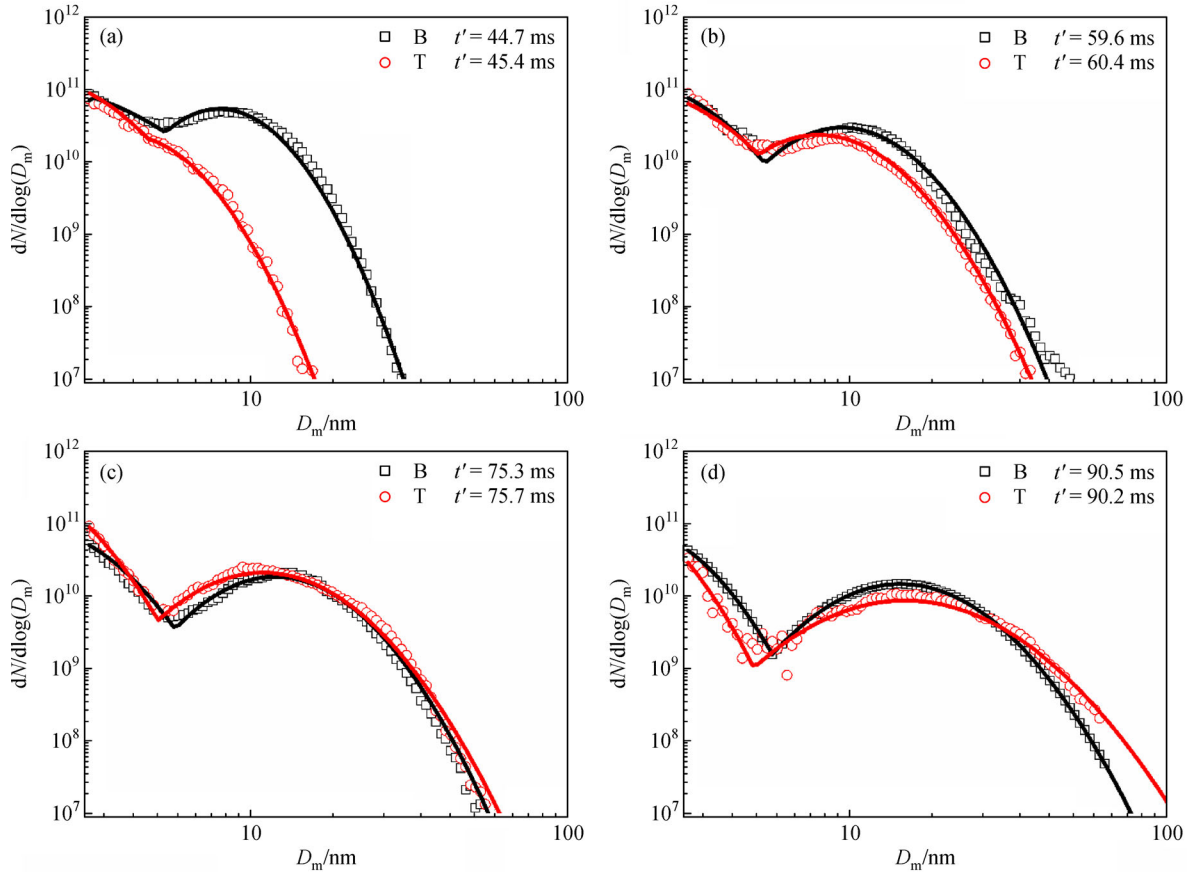

Fig. 5 Measured PSDFs for the two flames at different particle residence times (Symbols: experimental data; lines: bi-lognormal fitting data).

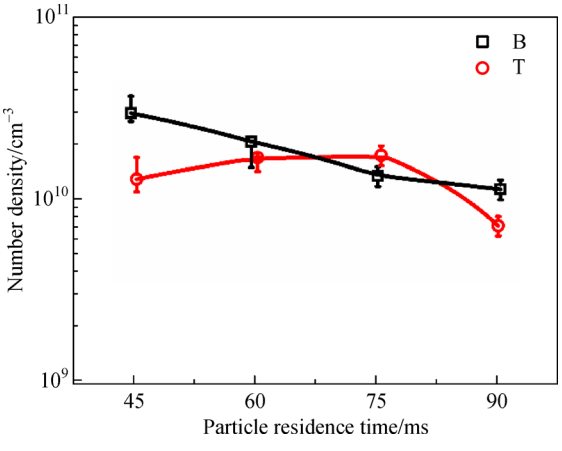

Fig. 6 Number density versus particle residence time (Symbols: experimental data; lines: drawn to guide the eye).

tion is not obvious at this time. The peak of total number density in the T flame suggests that the production of small-size particles is balanced with their consumption by particle accumulation. As t' is longer than 75 ms, the particle accumulation further increases and leads to a reduced number density of the T flame. For the B flame, the decrease in number density versus t' is observed. The reason for this is that the accumulation mode always plays a dominant role in these flames, i.e., the particle accumulation tendency is higher than the particle nucleation tendency at particle residence times longer than 45 ms. It could be inferred that the B flames also have the peak total number densities at shorter particle residence times, despite of the fact that those test conditions are not covered in this study.

The median mobility diameter of the particles in the accumulation mode as functions of particle residence time in the two flames are displayed in Fig. 7. With the particle residence times increasing, the median mobility diameter of the particles in the accumulation mode, $\langle D_m \rangle_2$, moves toward the larger size. This movement indicates the growth in particle size and the extension in distribution range. The $\langle D_m \rangle_2$ of the B flame are larger than that of the T flame at residence times between 45 and 70 ms, but is almost the same as that of the T flame at the residence time of 90 ms, indicating that the accumulation of the two flames are similar at a long residence time.

It might be assumed that the measured particles are spherical, and as such the soot volume fraction could be estimated by using

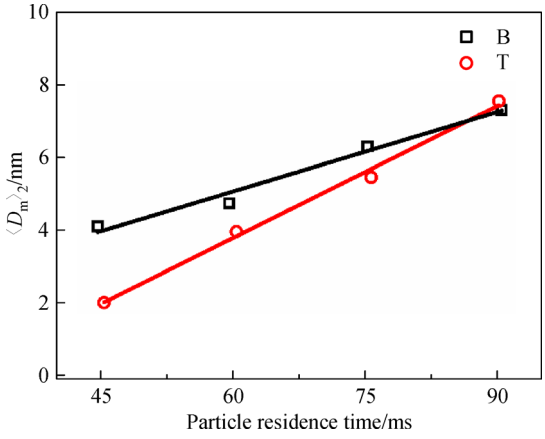

Fig. 7 Median mobility diameter of the particles in the accumulation mode versus particle residence time (Symbols: experimental data; lines: drawn to guide the eye).

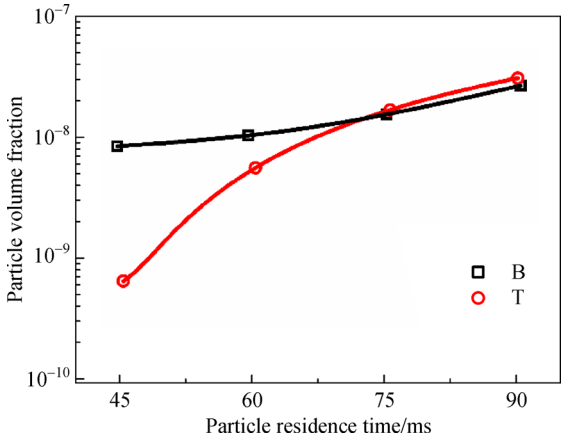

Fig. 8 Particle volume fraction versus particle residence time (Symbols: experimental data; lines: drawn to guide the eye).

$$F_v = \int_{D_{m,min}}^{D_m} \frac{\pi}{6} D_m^3 \frac{dN}{d\log D_m} d\log D_m, \quad (6)$$

where $D_{m,min}$ is the minimum mobility diameter that could be detected, which is defined as 2.5 nm here. The contribution of particles, whose mobility diameter is larger than 66.1 nm, to the number density is again estimated by the bi-lognormal distribution function fits. Figure 8 shows the variation of particle volume fraction as a function of particle residence time for the two flames. In general, the particle volume fraction monotonically increases with the particle residence times for both two flames due to the continuous particle generation. The particle volume fraction of the T flame is lower than that of the B flame at short particle residence times, but almost the same as that of the B flame at residence times over 75 ms. It can be inferred that the T flame has a stronger sooting tendency than the B flame when the accumulation mode dominates the PSDF at a given equivalence ratio.

Observing that the differences in the PSDFs of the B and T flames were large at low H_p values but small at large H_p values, a chemical kinetic study was conducted to illustrate this fuel effect. The calculated mole fraction profiles of acetylene and benzene are analyzed at H_p = 1.0 cm, which corresponds to the residence time of about 45 ms, as shown in Fig. 9. The B flame has a higher acetylene concentration than the T flame at the heights above the maximum temperature zone where large amounts of soot form and grow. This is consistent with the phenomenon the B flame has a stronger accumulation strengths. The T flame only has a slightly higher concentration of benzene at the heights above the maximum temperature zone, which is consistent with the relatively close nucleation tendency between the two flames.

4 Conclusions

Soot particle size evolution in premixed flames of benzene and toluene was experimentally investigated on the burner stabilized stagnation flame platform. The following conclusions are drawn based on the experimental results.

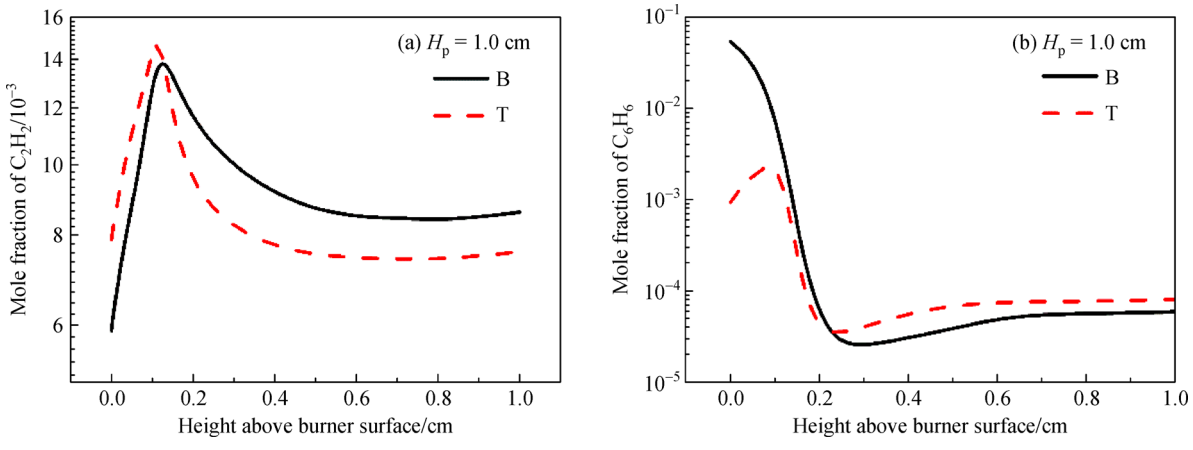

Fig. 9 Calculated mole fraction profiles of (a) acetylene and (b) benzene for the benzene and toluene flames at 1.0 cm.

At short particle residence times, the PSDFs of the benzene flame show bimodal distributions whereas the PSDFs the toluene flame show unimodal distributions, and the soot nucleation and particle growth in the benzene flame are stronger than those in the toluene flame. The benzene flame also has a higher number density than the toluene flame. As particle residence time increases, the PSDFs and particle volume fractions in the benzene and toluene flames become close, except the fact that the toluene flame shows a slightly wider particle size distribution range.

Acknowledgements This work was supported by the National Natural Science Foundation of China (Grant No. 51776124).

References

1. Brunekreef B, Holgate S T. Air pollution and health. Lancet, 2002, 360(9341): 1233–1242
2. Omidvarborna H, Kumar A, Kim D S. Recent studies on soot modeling for diesel combustion. Renewable & Sustainable Energy Reviews, 2015, 48: 635–647
3. Zhao F, Yang W, Zhou D, Yu W, Li J, Tay K L. Numerical modelling of soot formation and oxidation using phenomenological soot modelling approach in a dual-fueled compression ignition engine. Fuel, 2017, 188: 382–389
4. Reşitoğlu I A, Altinisik K, Keskin A. The pollutant emissions from diesel-engine vehicles and exhaust after treatment systems. Clean Technologies and Environmental Policy, 2015, 17(1): 15–27
5. EUR-Lex Website. Council Directive 91/441/EEC of 26 June 1991 amending Directive 70/220/EEC on the approximation of the laws of the Member States relating to measures to be taken against air pollution by emissions from motor vehicles. 1991, available at website of eur-lex.europa.eu
6. EUR-Lex Website. Commission Regulation (EU) No 459/2012 of 29 May 2012 amending Regulation (EC) No 715/2007 of the European Parliament and of the Council and Commission Regulation (EC) No 692/2008 as regards emissions from light passenger and commercial vehicles (Euro 6). 2012–06–01, available at website of eur-lex.europa.eu
7. Frenklach M, Clary D W, Gardiner W C Jr, Stein S E. Effect of fuel structure on pathways to soot. Symposium (International) on Combustion, 1986, 21(1):1067–1076
8. Wang Y, Makwana A, Iyer S, Linevsky M, Santoro R J, Litzinger T A, O'Connor J. Effect of fuel composition on soot and aromatic species distributions in laminar, co-flow flames. Part 1. Non-premixed fuel. Combustion and Flame, 2018, 189: 443–455
9. Sidebotham G W, Glassman I. Flame temperature, fuel structure, and fuel concentration effects on soot formation in inverse diffusion flames. Combustion and Flame, 1992, 90(3–4): 269–283
10. Butler J D, Crossley P. Reactivity of polycyclic aromatic hydrocarbons adsorbed on soot particles. Atmospheric Environment, 1981, 15(1): 91–94
11. Sobotowski R A, Butler A D, Guerra Z. A pilot study of fuel impacts on PM emissions from light-duty gasoline vehicles. SAE International Journal of Fuels and Lubricants, 2015, 8(1): 214–233
12. DeWitt M J, Corporan E, Graham J, Minus D. Effects of aromatic type and concentration in Fischer–Tropsch fuel on emissions production and material compatibility. Energy & Fuels, 2008, 22(4): 2411–2418
13. Short D Z, Vu D, Durbin T D, Karavalakis G, Asa-Awuku A. Components of particle emissions from light-duty spark-ignition vehicles with varying aromatic content and octane rating in gasoline. Environmental Science & Technology, 2015, 49(17): 10682–10691
14. Richter H, Granata S, Green W H, Howard J B. Detailed modeling of PAH and soot formation in a laminar premixed benzene/oxygen/argon low-pressure flame. Proceedings of the Combustion Institute, 2005, 30(1): 1397–1405
15. Bachmann M, Wiese W, Homann K H. Fullerenes versus soot in benzene flames. Combustion and Flame, 1995, 101(4): 548–550
16. Wei J, Song C, Lv G, Song J, Wang L, Pang H. A comparative study of the physical properties of in-cylinder soot generated from the combustion of n-heptane and toluene/n-heptane in a diesel engine. Proceedings of the Combustion Institute, 2015, 35(2): 1939–1946
17. Hansen N, Schenk M, Moshammer K, Kohse-Höinghaus K. Investigating repetitive reaction pathways for the formation of polycyclic aromatic hydrocarbons in combustion processes. Combustion and Flame, 2017, 180: 250–261
18. Camacho J. Development of a novel heterogeneous flow reactor-Soot formation and nanoparticle catalysis. Dissertation for the Doctoral Degree. Los Angeles: University of Southern California, 2013
19. Simmons B, Williams A. A shock tube investigation of the rate of soot formation for benzene, toluene, and toluene/n-heptane mixtures. Combustion and Flame, 1988, 71(3): 219–232
20. Ergut A, Levendis Y A, Richter H, Howard J B, Carlson J. The effect of equivalence ratio on the soot onset chemistry in one-dimensional, atmospheric-pressure, premixed ethylbenzene flames. Combustion and Flame, 2007, 151(1–2): 173–195
21. Gigone B, Karatas A E, Gülder Ö L. Soot aggregate morphology in coflow laminar ethylene diffusion flames at elevated pressures. Proceedings of the Combustion Institute, 2019, 37(1): 841–848
22. Maricq M M. A comparison of soot size and charge distributions from ethane, ethylene, acetylene, and benzene/ethylene premixed flames. Combustion and Flame, 2006, 144(4): 730–743
23. Tang Q, Ge B, Ni Q, Nie B, You X. Soot formation characteristics of n-heptane/toluene mixtures in laminar premixed burner-stabilized stagnation flames. Combustion and Flame, 2018, 187: 239–246
24. Abid A D, Tolmachoff E D, Phares D J, Wang H, Liu Y, Laskin A. Size distribution and morphology of nascent soot in premixed ethylene flames with and without benzene doping. Proceedings of the Combustion Institute, 2009, 32(1): 681–688
25. Echavarria C A, Sarofim A F, Lighty J A S, D'Anna A. Evolution of soot size distribution in premixed ethylene/air and ethylene/benzene/air flames: experimental and modeling study. Combustion and Flame, 2011, 158(1): 98–104
26. Lin B, Gu H, Guan B, Han D, Gu C, Huang Z, Lin H. Size evolution of soot particles from gasoline and n-heptane/toluene blend in a burner stabilized stagnation flame. Fuel, 2017, 203: 135–144
27. Shaddix C R. Correcting thermocouple measurements for radiation loss: a critical review. Aibuquerque, NM, 1999, HTD99–HT282
28. Peterson R C, Laurendeau N M. The emittance of yttrium-beryllium

oxide thermocouple coating. Combustion and Flame, 1985, 60(3): 279–284

29. Shao C, Guan B, Lin B, Gu H, Gu C, Li Z, Lin H, Huang Z. Effect of methane doping on nascent soot formation in ethylene-based laminar premixed flames. Fuel, 2016, 186: 422–429
30. Lin H, Gu C, Camacho J, Lin B, Shao C, Li R, Gu H, Guan B, Wang H, Huang Z. Mobility size distributions of soot in premixed propene flames. Combustion and Flame, 2016, 172: 365–373
31. Smooke M D, Puri I K, Seshadri K A. A comparison between numerical calculations and experimental measurements of the structure of a counterflow diffusion flame burning diluted methane in diluted air. Symposium (International) on Combustion, 1988, 21(1): 1783–1792
32. Kee R J, Miller J A, Evansl G H, Dixon-Lewis G. A computational model of the structure and extinction of strained, opposed flow, premixed methane-air flames. Symposium (International) on Combustion, 1989, 22(1): 1479–1494
33. Lutz A E, Kee R J, Grcar J F, Rupley F M. OPPDIF: a Fortran program for computing opposed-flow diffusion flames. Sandia National Laboratories, Albu-querque, New Mexico, 1996
34. Zhao B, Yang Z, Li Z, Johnston M V, Wang H. Particle size distribution function of incipient soot in laminar premixed ethylene flames: effect of flame temperature. Proceedings of the Combustion Institute, 2005, 30(1): 1441–1448
35. Abid A D, Heinz N, Tolmachoff E D, Phares D J, Campbell C S, Wang H. On evolution of particle size distribution functions of incipient soot in premixed ethylene–oxygen–argon flames. Combustion and Flame, 2008, 154(4): 775–788
36. Waldmann L. The force of a non-homogeneous gas on small suspended spheres. Zeitshrift fur Naturforschung Section A—A Journal of Physical Sciences, 1959, 14a: 589–599
37. Li Z, Wang H. Drag force, diffusion coefficient, and electric mobility of small particles II: application. Physical Review. E, 2003, 68(6): 061207
38. Lai F S, Friedlander S K, Pich J, Hidy G M. The self-preserving particle size distribution for Brownian coagulation in the free-molecule regime. Journal of Colloid and Interface Science, 1972, 39(2): 395–405